Automatic Reconstruction of Deep Brain Stimulation Lead Trajectories From CT Images Using Tracking and Morphological Analysis

Wanxuan Sang, Zhiwen Xiao, Tiangang Long, Changqing Jiang, *Member, IEEE*, and Luming Li, *Member, IEEE*

***Abstract*— Deep brain stimulation (DBS) is an effective treatment for neurological disorders, and accurately reconstructing the DBS lead trajectories is crucial for MRI compatibility assessment and surgical planning. This paper presents a novel fully automated framework for reconstructing DBS lead trajectories from postoperative CT images. The leads were first segmented by thresholding, but would be fused together somewhere. Mean curvature analysis of multi-layer CT number isosurfaces was introduced to effectively address lead fusion, due to the different topological characteristics of the isosurfaces in and out of the fusion regions. The position of electrode contacts was determined through morphological analysis to get the starting point and the initial direction for trajectory tracking. The next trajectory point was derived by calculating the weighted average coordinates of the candidate points, using the distance from the current estimated trajectory and the CT number as weights. This method has demonstrated high accuracy and efficiency, successfully and automatically reconstructing complex bilateral trajectories for 13 patient cases in less than 10 minutes with errors less than 1 mm. This work overcomes the limitations of existing semi-automatic techniques that require extensive manual intervention. It paves the way for optimizing DBS lead trajectory to reduce tissue heating and image artifacts, which will contribute to neuroimaging studies and improve clinical outcomes. Code for our proposed algorithm is publicly available on Github.**

***Index Terms*— CT number, deep brain stimulation, mean curvature, trajectory tracking.**

Received 16 July 2024; revised 18 September 2024; accepted 5 November 2024. Date of publication 7 November 2024; date of current version 14 November 2024. This work was supported in part by the National Natural Science Foundation of China under Grant 52477234 and Grant T2488101 and in part by the National Key Research and Development Program of China under Grant 2021YFC2400200. *(Corresponding author: Changqing Jiang.)*

This work involved human subjects or animals in its research. Approval of all ethical and experimental procedures and protocols was granted in part by Tsinghua University Science and Technology Ethics Committee (Medicine) under Application No. THU01-20230188, in part by the Medical Ethics Committee of Beijing Tsinghua Changgung Hospital under Application No. 22491-4-01, in part by the Ethics Committee of Peking Union Medical College Hospital, Chinese Academy of Medical Sciences under Application No. K4055, and in part by the Ethics Committees of Tiantan Hospital, Peking Union Medical College Hospital, and Qilu Hospital under Application No. NCT02937727.

Wanxuan Sang, Tiangang Long, and Changqing Jiang are with the National Engineering Research Center of Neuromodulation, School of Aerospace Engineering, Tsinghua University, Beijing 100084, China (e-mail: jiangcq13@tsinghua.edu.cn).

Zhiwen Xiao is with the Department of Aeronautics and Astronautics Engineering, School of Aerospace Engineering, Tsinghua University, Beijing 100084, China.

Luming Li is with the National Engineering Research Center of Neuromodulation, School of Aerospace Engineering, and the IDG/McGovern Institute for Brain Research, Tsinghua University, Beijing 100084, China.

Digital Object Identifier 10.1109/TNSRE.2024.3493862

I. Introduction

DEEP brain stimulation (DBS) is a neuromodulation technology that has gained significant recognition for its effectiveness in treating drug-resistant neurological and psychiatric disorders [1]. The number of patients who have undergone DBS worldwide exceeds 160,000 and is increasing yearly [2]. It's estimated that 66-75% of these patients will need an MRI within 10 years after implantation [3]. However, radiofrequency (RF) pulses during MRI may induce high currents in DBS electrode leads and extension cables [4]. This can induce local tissue heating [5], and also cause artifacts that reduce the quality of MRI images [6]. These effects not only increase the risk of patient injury, but also interfere with electrode localization and lesion diagnosis.

Studies have shown that optimizing the DBS lead trajectory can significantly reduce tissue heating [7], [8], [9] and image artifacts [10] during 1.5 T and 3 T MRI, providing a new strategy to enhance both the MRI safety and image quality of DBS patients. The precise reconstruction and assessment of the realistic DBS lead trajectories are essential for applying these research findings to clinical practice.

The DBS leads can be segmented by thresholding computed tomography (CT) images of patients, since the leads are mainly composed of metal. Golestanirad et al. [11] used a skeletonization algorithm followed by a smooth curve-fitting algorithm to estimate the centerline of the lead, and then adjusted the intersecting segments of the centerline manually to eliminate self-intersections. Guerin et al. [12] proposed an automatic topology correction algorithm aimed at removing self-intersections and curvature violations. But this algorithm required manual connection of centerline segments to form a preliminary trajectory, still relying on human judgment of

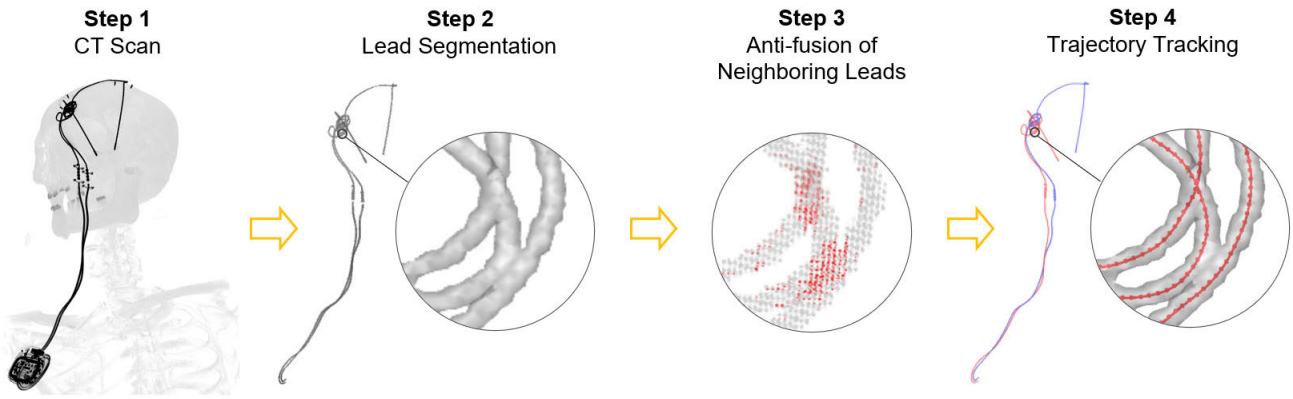

Fig. 1. The process for automatic reconstruction of the DBS lead trajectory from CT images. Step 1: Perform a spiral CT scan of the DBS implantation region. Step 2: Segment the leads based on density and volume ratio. Step 3: Apply mean curvature analysis to the CT number isosurface for anti-fusion of neighboring leads. Step 4: Reconstruct the trajectory of the leads through point-by-point tracking.

orientation and connectivity. Golestanirad et al. [13], [14] switched to directly manually extracting trajectory lines in CAD software in their subsequent studies, which was difficult to operate and ensure accuracy.

The immediate reason why these studies failed to automatically reconstruct the trajectories is that the segmented leads cannot correctly reflect the topology. The DBS lead trajectories involve a large number of intersecting and overlapping loops, especially in the extracranial region. Unfortunately, the CT numbers of the lead are not globally uniform in CT images. Thus, A high threshold for segmentation results in disconnected leads, while a low threshold results in blurred leads and fusion of neighboring electrodes leads. In addition, the diameter of the wires in the lead is only 1.5 times the CT resolution which makes the problem more difficult.

This paper proposes a novel framework for trajectory reconstruction, whose key components are anti-fusion of neighboring leads and trajectory tracking. The convexity and concavity derived from the mean curvature of the CT number isosurface can help to solve the topology mistakes of the segmented leads. After that, the whole trajectory starts from the electrode contact, and then the next trajectory point is calculated by the weighted average of the CT numbers and whether it belongs to the lead or not.

The proposed method exhibits several significant advantages over existing techniques. It is fully automated and highly efficient, capable of reconstructing a trajectory within five minutes. It also has a high accuracy and success rate, successfully extracting trajectories for all 13 patients with bilateral implants, with errors of less than 1 mm. This method lays the foundation for optimizing DBS trajectories, enhancing MRI safety, and reducing MRI image artifacts.

II. Method

Fig. 1 illustrates the process of automatically reconstructing DBS trajectories from CT images. First, A spiral CT scan was performed (Step 1), followed by the segmentation of the DBS leads (Step 2). Subsequently, mean curvature analysis was applied to the CT number isosurface to facilitate the separation of adjacent leads (Step 3). The final step (Step 4) involved trajectory tracking, initiating from the electrode contacts and tracing the trajectory point by point. The code is available at https://github.com/Wanxuan-Sang/DBS_lead_trajectory_from_CT.

A. CT Scan and Lead Segmentation

Thirteen patients with bilateral deep brain stimulators implanted were selected as study subjects, and they all provided informed consent. This study was approved by Tsinghua University Science and Technology Ethics Committee (Medicine) under Application THU01-20230188, Medical Ethics Committee of Beijing Tsinghua Changgung Hospital under Application No. 22491-4-01, Ethics Committee of Peking Union Medical College Hospital, Chinese Academy of Medical Sciences under Application No. K4055, and Ethics Committees of Tiantan Hospital, Peking Union Medical College Hospital, and Qilu Hospital under Application NCT02937727. Spiral CT scan was performed using either the United Imaging uCT 760 CT scanner or the GE Revolution CT scanner with the Extended HU mode on. The scanning range extended from the top of the skull to the inferior border of the implanted stimulator, using a 120 kV tube voltage at 180-450 mA tube current modulation. The source image was reconstructed using the bone kernel algorithm with a slice thickness of 0.625 mm, slice spacing equal to the slice thickness and a matrix size of 512×512.

The CT image is composed of multiple layers of slices, each of which is a square matrix. Each element of the matrix represents a voxel and contains a CT number that reflects the density information [15], [16]. The DBS lead consists mainly of a polyurethane tubing containing four spiral wound platinum/iridium wires [17], whose CT numbers are quite higher than that of body tissues. As the 0.9 mm wire diameter is only 1.5 times the voxel size, the CT image was up-sampled by a factor of 2 along all dimensions through linear interpolation. Then, a threshold of 5000 was set to segment the voxels of metal. Among them, the voxels of the leads were always separated from those of screws and implantable pulse generators. Due to the slender geometry of the lead, the volumetric ratio of connected voxels to their bounding box

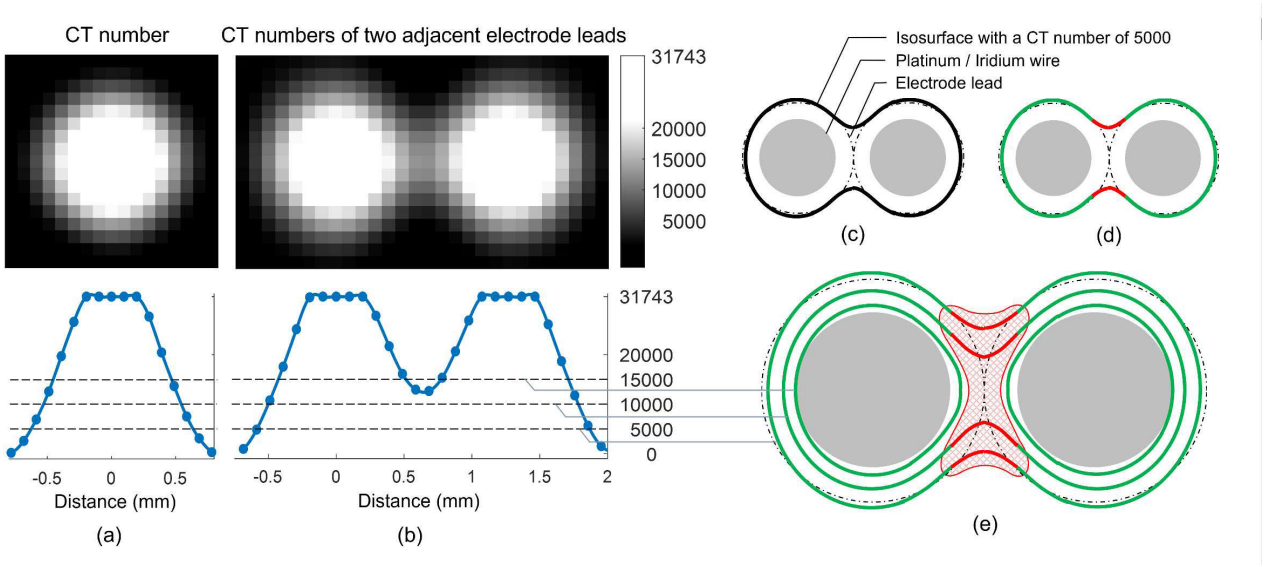

Fig. 2. Fusion and anti-fusion of neighboring leads. (a) CT numbers in the cross-section and on the centerline of the cross-section of an electrode lead. (b) CT numbers in the cross-section and on the centerline of the cross-section of two adjacent leads. (c) The cross-sections of two adjacent leads after thresholding segmentation. (d) The mean curvature of the cross-sections isosurface for two adjacent leads. (e) The principle for determining the fusion regions by mean curvature analysis of multi-layer isosurfaces.

is quite low. As a result, the voxels of leads can be preserved based on this ratio. These voxels were also converted into a point cloud that stored their original coordinates.

B. Anti-Fusion of Neighboring Leads

During DBS implantation, the excess extracranial DBS leads were looped under the patient's scalp, often in close proximity to each other. Fig. 2 (a) and 2(b) show the CT numbers of an electrode lead (L301C, Beijing PINS Medical Co., Ltd., China) and two adjacent leads in the cross-section and on the centerline of the cross-section. These leads were collinear with the CT rotation axis and the CT images were reconstructed with the minimum field of view.

For the single lead, it can be observed that the CT numbers gradually increase towards the center of the lead (reaching a maximum value of 31743, which corresponds to the upper limit of the GE system), with no abrupt transition at the lead-background interface. The lead segmented with a threshold of 5000 corresponds to its actual diameter. For two adjacent leads, the CT numbers around the contact area increased. As evident from the isosurface with a CT number of 5000 in Fig. 2(c), the leads would be fused together after threshold segmentation, complicating the determination of the lead direction during trajectory tracking. Although using a higher threshold can avoid fusion, it may result in the segmented leads becoming fragmented. This issue arises from CT numbers in certain regions being below the normal level, which is influenced by the angle at which the leads are tilted relative to the CT rotation axis [18].

The mean curvature of the isosurface can help to identify the fusion regions. As shown in Fig. 2(d), the isosurface in the fusion regions is concave and marked as red, in contrast to the green convex isosurface out of the fusion regions. The mean curvature H characterizes the extrinsic measure of surface shape [19], defined as the mean of maximum and minimum curvatures at a given surface point. Concave surfaces satisfy $H < 0$, while convex surfaces satisfy $H > 0$. The mean curvature is calculated using Algebraic Point Set Surfaces (APSS), a surface definition method that provides reliable estimates of average curvature and robustly handles sharp features and boundaries [20].

Multi-layer isosurfaces at CT numbers ranging from 5000 to 15000, in intervals of 1000, were used to identify the fusion regions, as depicted in Fig. 2(e). The fusion regions were determined as the union of multiple cubics, centered on points where $H < 0$ on the isosurfaces, with each cube the same size as a CT voxel.

C. Trajectory Tracking

1) Start Point Determination: Trajectory tracking starts from the contact side of the lead along the initial direction. The position of the contact can be directly determined either by its unique CT number [21] or by its morphology. Fig. 3(a) presents the morphological process in three stages: the first part shows the initial voxels of the leads, the second part shows the voxels with simplified topology structure after dilation and erosion, and the third part depicts the skeleton of the voxels and marks two contacts. Specifically, dilation was used to expand and connect adjacent sections of the leads, resulting in a single connected geometry, and erosion was applied to refine the structure [22], [23]. Subsequently, skeletonization was performed to extract the central line of the leads, which was then pruned to eliminate any remaining minor branches [24], [25]. Finally, three endpoints of the skeleton were identified and the two closest endpoints among them were on the contact side.

Since the electrode leads were implanted through a straight guide tube, the lead segments within the spheres centered on each skeleton endpoint with radii of 5 mm and 10 mm were straight. Thus, the point cloud centers $\boldsymbol{C}_0$ and $\boldsymbol{C}_1$ of the lead segments were located on the center line of the lead. The

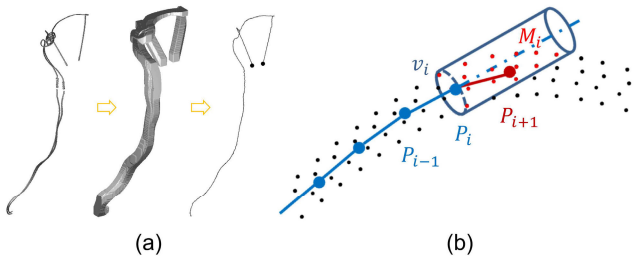

Fig. 3. Trajectory tracking process. (a) Determine the start point on the contact side of the lead mainly by morphology. (b) Calculate the next trajectory point P_{i+1} using a weighted averaged method based on the point cloud in front of the current trajectory point P_i.

start point $\boldsymbol{P}_0$ was defined as $\boldsymbol{C}_0$- d_{mp}·$\boldsymbol{s}_0$, where $\boldsymbol{s}_0$ was a unit vector representing the direction of $\boldsymbol{C}_0$- $\boldsymbol{C}_1$ and d_{mp} was the maximum projection distance along -$\boldsymbol{s}_0$ between a point in the point cloud and $\boldsymbol{C}_0$.

2) Overall Idea of Trajectory Point Calculation: The trajectory was considered as a polyline with vertexes on the center line of the lead. During trajectory tracking, each trajectory point P_i and the point cloud ahead was used to calculate the next trajectory point $\boldsymbol{P}_{i+1}$. The direction of $\boldsymbol{P}_{i+1}$ - $\boldsymbol{P}_i$ was represented by a unit vector s_i, and the step length l was set to 0.5 mm, as shown in (1).

$$\boldsymbol{P}_{i+1} = \boldsymbol{P}_i + l \cdot \boldsymbol{s}_i \tag{1}$$

As illustrated in Fig. 3(b), a cylindrical region was taken as the vision field v_i of $\boldsymbol{P}_i$, representing the region referenced in the calculation of $\boldsymbol{P}_{i+1}$. It was defined with a base center at $\boldsymbol{P}_i$, a radius equal to lead radius, a height of $2l$, and an centerline c_i parallel to $\boldsymbol{s}_{i-1}$. As long as l is short enough, it is expected that $\boldsymbol{P}_{i+1}$ should fall in v_i. The lead points in v_i were denoted as $\boldsymbol{M}_i$, each of which was denoted as $M_{i,j}$. The coordinates of $\boldsymbol{M}_{i,j}$ relative to $\boldsymbol{P}_i$ were weighted averaged with weights w_j to obtain $\boldsymbol{s}_i$, as shown in (2).

$$\boldsymbol{s}_i = \frac{\sum_{\boldsymbol{M}_{i,j} \in \boldsymbol{M}_i} (\boldsymbol{M}_{i,j} - \boldsymbol{P}_i) \times w_j}{\left| \sum_{\boldsymbol{M}_{i,j} \in \boldsymbol{M}_i} (\boldsymbol{M}_{i,j} - \boldsymbol{P}_i) \times w_j \right|} \tag{2}$$

The global minimum distance $D_{\min}$ between any two segments of the patient trajectories was denoted as

$$D_{\min} = \min \left(D\left(S_m^1, S_n^1\right), D\left(S_k^2, S_l^2\right), D\left(S_m^1, S_k^2\right) \right) \tag{3}$$

S_m^1 is segment m of the trajectory 1, and S_n^2 is segment n of the trajectory 2. Indices m, n run over the number of segments in trajectory 1, and indices k, l run over the number of segments in trajectory 2. D is the segment–segment distance defined as the minimum distance between any two points belonging to these two segments as in [12].

3) Weights: The weight w_j was composed of three components, taking into account the influence of position, CT number, and the fusion regions:

$$w_j = w_{d,j} \times w_{\mathrm{CT},j} \times w_{\mathrm{fusion},j}. \tag{4}$$

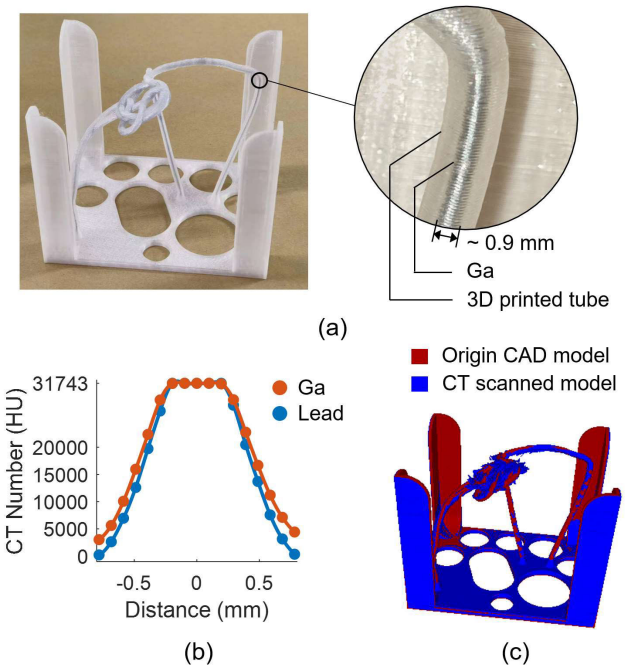

Fig. 4. Validation model. (a) Create a validation model from the patient trajectories. (b) CT numbers on the centerline of the cross-section of liquid metal gallium (Ga) and an electrode lead. (c) CT scan the validation model and align with the origin CAD model.

Considering that the actual trajectory was a smooth curve, the angle between $\boldsymbol{s}_i$ and $\boldsymbol{s}_{i+1}$ was small, and $\boldsymbol{P}_{i+1}$ was close to the centerline c_i. The closer a point was to c_i, the higher the weight $w_{d,j}$ was. The distance from $\boldsymbol{M}_{i,j}$ to c_i was denoted as d_j. An inverse distance weighting function [26] was used to define d_j, which includes an upper limit to prevent divergence, specifically:

$$w_{d,j} = 1/\max(d_j, 0.1). \tag{5}$$

A higher weight $w_{\mathrm{CT},j}$ was assigned to the point with a higher CT number, as the CT numbers of the lead increase toward the center, denoted as:

$$w_{\mathrm{CT},j} = \frac{\text{CT number}_j}{5000}. \tag{6}$$

Additionally, points in the fusion regions were given a weight of 0, while others were given a weight of 1, as shown in (7).

$$w_{\mathrm{fusion},j} = \begin{cases} 0 & \text{if } M_j \in \text{fusion regions} \\ 1 & \text{if } M_j \notin \text{fusion regions} \end{cases} \tag{7}$$

D. Experimental Validation

Fig. 4(a) shows a validation model used to assess the accuracy of the trajectory reconstruction method. The model consisted of a frame and hollow tubes shaped according to the patient trajectory T_{p}, and was produced by a fused deposition modeling (FDM) 3D printer with a 0.4 mm nozzle and a 0.2 mm layer height. Liquid metal gallium (Ga) was filled inside the tubes to represent the high-density spiral wires of the DBS lead, thus overcoming the difficulty of inserting metal

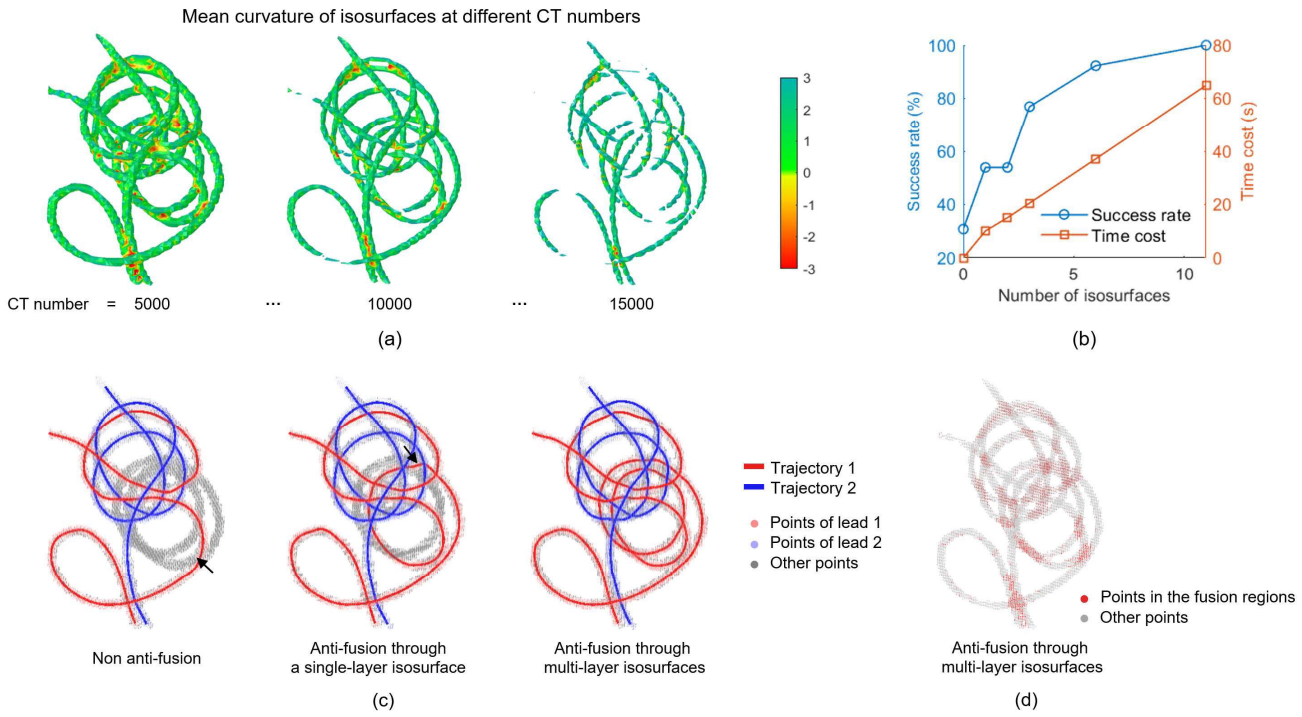

Fig. 5. (a) The mean curvature of isosurfaces at different CT numbers where the leads were fused together. (b) The effect of the number of isosurfaces on the time cost of fusion regions identification and the success rate of reconstruction. (c) Trajectories reconstructed without anti-fusion, with anti-fusion through a single-layer isosurface, and with anti-fusion through multi-layer isosurfaces. (d) Points in the fusion regions that are assigned a weight of zero.

wires into the narrow tubes. Fig. 4(b) compares the CT number distribution of Ga and leads. It can be seen that they are quite similar and both follow the same pattern of increasing CT numbers towards the center, indicating that Ga serves as a reasonable substitute.

The validation trajectory T_{v} was reconstructed following the process described above. The surface of the validation model obtained from the CT image was aligned with the surface of the origin CAD model using MeshLab (version 2023.12, Visual Computing Lab, ISTI-CNR, Italy), as shown in Fig. 4(c). The align matrix was used to eliminate the rigid transformation between T_{v} and T_{p}.

The distance D'_n between T_{p} and segment n of T_{v} was calculated to assess the error level of the reconstruction method, denoted as

$$D'_n = \min\left(D\left(S_m, S'_n\right)\right). \tag{8}$$

S_m is segment m of T_{p}, and S'_n is segment n of the T_{v}. Index m runs over the number of segments in T_{v}. The maximum distance $D'_{\max}$ between T_{p} and T_{v} was denoted as

$$D'_{\max} = \max\left(D'_n\right), \tag{9}$$

where index n runs over the number of segments in T_{v}.

III. Results

A. Effects of Anti-Fusion

Fig. 5(a) shows the mean curvature distributions on CT number isosurfaces at 5000, 10000, and 15000, where the leads were fused together and trajectory tracking faces great challenges.

As illustrated in Fig. 5(b), the number of isosurfaces at CT numbers ranging from 5000 to 15000 affects the success rate of reconstruction by influencing the identification of the fusion regions. Additionally, the time cost of identification is plotted. Without anti-fusion, the success rate of reconstruction was only 31%. With anti-fusion through a single-layer isosurface at 5000, the success rate improved to 54%. With anti-fusion through multi-layer isosurfaces as mentioned above, a 100% success rate was achieved.

Fig. 5(c) illustrates the trajectories reconstructed using those three methods. In this case, the impact of the fusion regions was obvious, resulting in trajectory 1 being lost at the position marked by the arrow. Anti-fusion though single-layer isosurface and multi-layer isosurfaces reduced this impact gradually. Fig. 5(d) shows the points in the fusion regions, which were assigned a weight of zero during trajectory tracking.

B. Reconstructed Trajectories for Different Patients

Fig. 6 presents 26 reconstructed trajectories from 13 patients with bilateral DBS implantation, and all of them are complex trajectories with coils. For patients 1-10, only the electrode lead trajectory was shown because only the head was scanned. For the other 3 patients, both the electrode lead and the extension cable were reconstructed. The reconstruction was performed on a personal computer running Microsoft Windows 10 and configured with an Intel(R) Core(TM) i7-1065G7 CPU @ 1.30GHz 1.50 GHz

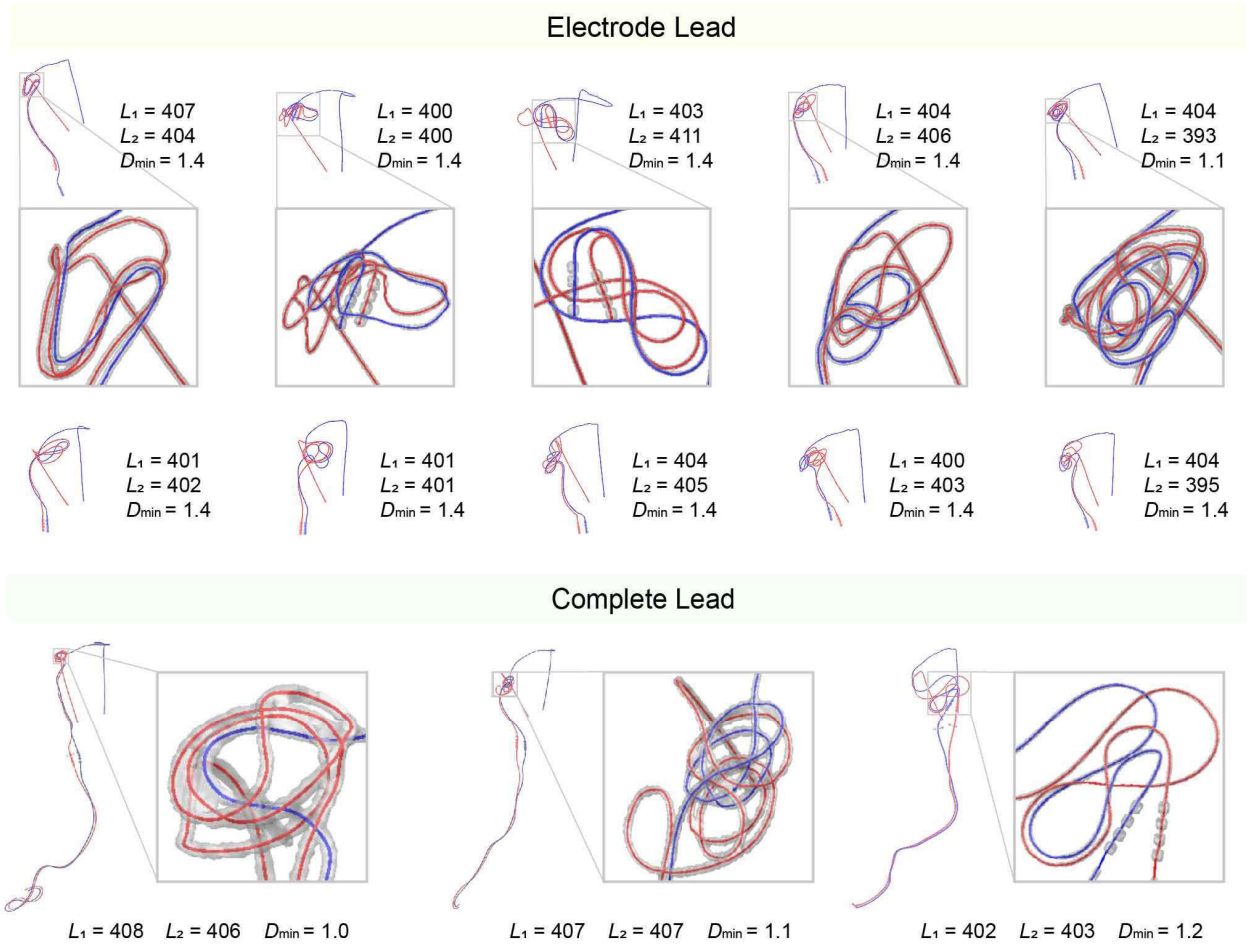

Fig. 6. Reconstructed trajectories of different patients, including localized magnification of coiled lead, the length of electrode lead trajectories L_1 and L_2, and the minimum distance $D_{\min}$ between two lead trajectories (all quantities are expressed in mm). In cases 1-10, only the head was scanned, so only the electrode lead trajectories are shown. Cases 11-13 show the trajectory of complete lead including the electrode lead and extension cable.

processor. The reconstruction time for each patient was less than 10 minutes.

Fig. 6 also lists the length of the electrode lead trajectory and the global minimum distance $D_{\min}$ between any two segments of the patient trajectories as defined in (3). The average length was 403 ± 3 mm, with a minimum of 393 mm and a maximum of 411 mm, a deviation of less than 3% from the theoretical lead length of 400 mm. Most $D_{\min}$ are 1.4 mm, while the smallest is 1.0 mm. Compared to the electrode lead diameter of 1.3 mm and the wire diameter of 0.9 mm, these results are acceptable considering the potential deformation of the lead under external forces, these results are acceptable.

C. Validation Results

Fig. 7 presents the results of the experimental validation. Fig. 7(a) shows 10 patient trajectories T_{p}s and the corresponding validation trajectories T_{v}s. The two lead trajectories of a patient were manually separated in order to be seen clearly. T_{v} and T_{p} are quite close, and the left T_{v} and the right T_{v} are not confused with each other. Thus, the correctness of the reconstruction method is confirmed.

Fig. 7(b) provides local details at the position where the maximum distance $D'_{\max}$ between T_{p} and T_{v} is the largest among 10 cases. The largest $D'_{\max}$ is 0.7 mm, only half of the lead diameter, which shows the high accuracy of the reconstruction method. The statistical analysis of the distance D'_n between T_{p} and segment n of T_{v} is shown in Fig. 7(c). The distance is quite smaller than that of [12], indicating a lower error level of this method.

IV. Discussion

A large number of DBS patients worldwide require MRI, but there are still many issues that need to be addressed. Tissue heating and image artifacts can be significantly reduced by changing the DBS lead trajectory. In this study, we presented a novel, fully automated framework for reconstructing DBS lead trajectories from postoperative CT images using tracking and morphological analysis. The key contributions include anti-fusion strategies for DBS leads, a robust trajectory tracking method based on weighted average coordinates, and a validation method using liquid metal gallium. Table I summarizes comparisons of this study with related studies.

CT numbers contain a great deal of information that has not been given enough attention before. Fig. 2 shows the CT

TABLE I
COMPARISON OF THIS STUDY AND RELATED STUDIES

Study	Year	Manual Operation	Number of trajectories	Succuss Rate	Time Consumed	Length of Reconstructed electrode lead trajectories
[11]	2017	Adjusting the intersecting segments of the center line.	9	\	\	38 - 55 cm
[12]	2018	Connecting the branches corresponding to the left and the right DBS leads.	6	83%	< 5 h	\
[13]	2019	Reconstructing lead trajectory lines from 3D lead surfaces.	18	\	\	\
This study	2024	None.	26	100%	< 10 min	393 - 411 mm

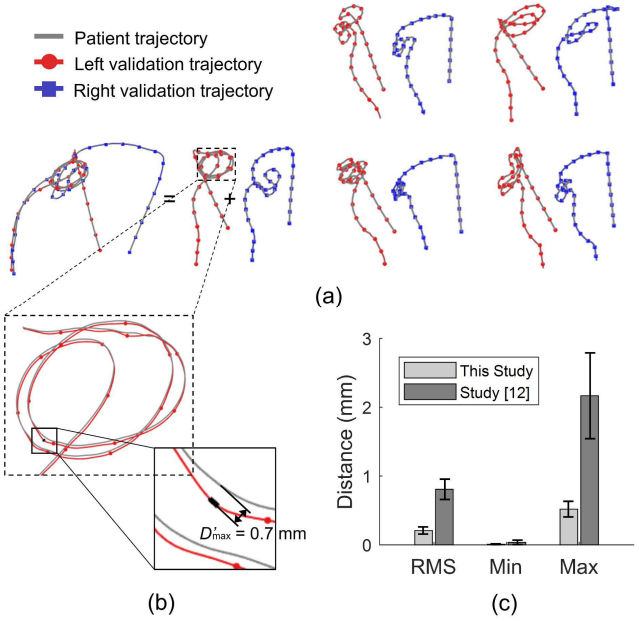

Fig. 7. Results of the experimental validation. (a) 10 patient trajectories and the corresponding validation trajectories. (b) Local details at the position where D'_{max} is the largest among 10 cases. (c) The root mean square (RMS), minimum and maximum of the distance D'_n between the patient trajectory and segment n of the validation trajectory in 10 cases. The bar graph shows the averaged quantities and the error bars show the standard deviation.

number distribution of an electrode lead in the cross-section. The closer to the center, the higher the CT number. Since the trajectory is the centerline of the lead, the CT number was used to improve the accuracy of trajectory reconstruction. The weight based on CT number ensures the correctness when there are no fusion regions.

CT numbers around the contact area of two adjacent leads increased. Thus, the leads were fused together after threshold segmentation, which would generate skeletons with topological errors after skeletonization [12]. The CT number isosurface in the fusion regions is concave, in contrast to the convex isosurface out of the fusion region. The extrinsic measure of surface shape can be characterized by mean curvature. The fusion regions were obtained by globally analyzing the mean curvature of the multi-layer isosurfaces. Excluding fusion regions simplified the problems to be faced during trajectory tracking.

Trajectory tracking is based on local information such as position and CT number, and treats the trajectory as a polyline. Each lead point in the cylindrical vision field of the trajectory point was weighted average to determine the next direction. The idea of trajectory tracing is somewhat similar to manual reconstruction, but it uses more internal information of the lead, making reconstruction more accurate and faster.

Injecting liquid metal Ga into 3D-printed models offers a practical solution for accurately replicating complex patient trajectories. The use of liquid metal provides a novel approach to simulating the high-density spiral wires of DBS leads. The similarity in CT number distributions between Ga and the leads, as demonstrated in Fig. 4(b), supports the effectiveness of this substitution.

The accuracy and efficiency of our automated framework hold significant implications. Reliable reconstruction is critical for ensuring the safety and effectiveness of MRI. Safe scanning conditions can be individualized based on the patient's DBS lead trajectory. Based on lots of CT images, a database can be built up for future studies on the impact and further improvements of trajectory. This method can also be generalized to other implants with leads and generate greater clinical value.

While the results of our method are promising, we must recognize its limitations and the scope for further advancements in future research. Due to the thin wire, the CT resolution should be sufficiently high. The impact of CT imaging paraments can be studied in the future, which may help to determine a wider range of parameters. Moreover, the small differences in CT numbers between Ga and the leads might slightly influence the validation accuracy, which could be explored in future research. Additionally, only 26 trajectories were reconstructed, which was limited for validation of methods and for future study about the influence of trajectory. Future research should aim to apply the method across a larger and more diverse patient population. Finally, it is possible to combine the advantages of artificial intelligence based on a database built by our method in the future.

V. CONCLUSION

This study presented a novel, fully automated framework to accurately reconstruct the DBS lead trajectories from postoperative CT images. The approach demonstrated high accuracy and efficiency, with an error of less than 1 mm and a processing time under 10 minutes for bilateral trajectories across 13 patient cases. This robust trajectory reconstruction

lays the foundation for optimizing DBS lead implantation to enhance MRI safety and imaging quality.

ACKNOWLEDGMENT

The authors would like to thank Chen Yao, Huiling Yu, Feng Zhang, Yingbing Hu, Zhaoyuan Zhang, and Peishan Li from the National Engineering Research Center of Neuromodulation, Tsinghua University for their help in CT data collection.

REFERENCES

[1] E. B. Montgomery and J. T. Gale, "Mechanisms of action of deep brain stimulation (DBS)," *Neurosci. Biobehavioral Rev.*, vol. 32, no. 3, pp. 388–407, Jan. 2008.

[2] A. M. Lozano et al., "Deep brain stimulation: Current challenges and future directions," *Nat. Rev. Neurol.*, vol. 15, no. 3, pp. 148–160, Mar. 2019.

[3] S. Falowski, Y. Safriel, M. P. Ryan, and L. Hargens, "The rate of magnetic resonance imaging in patients with deep brain stimulation," *Stereotactic Funct. Neurosurgery*, vol. 94, no. 3, pp. 147–153, Jun. 2016.

[4] A. Boutet et al., "Improving safety of MRI in patients with deep brain stimulation devices," *Radiology*, vol. 296, no. 2, pp. 250–262, Aug. 2020.

[5] L. M. Angelone, J. Ahveninen, J. W. Belliveau, and G. Bonmassar, "Analysis of the role of lead resistivity in specific absorption rate for deep brain stimulator leads at 3T MRI," *IEEE Trans. Med. Imag.*, vol. 29, no. 4, pp. 1029–1038, Apr. 2010.

[6] C. R. Camacho, D. B. Plewes, and R. M. Henkelman, "Nonsusceptibility artifacts due to metallic objects in MR imaging," *J. Magn. Reson. Imag.*, vol. 5, no. 1, pp. 75–88, Jan. 1995.

[7] K. B. Baker, J. Tkach, J. D. Hall, J. A. Nyenhuis, F. G. Shellock, and A. R. Rezai, "Reduction of magnetic resonance imaging-related heating in deep brain stimulation leads using a lead management device," *Operative Neurosurgery*, vol. 57, no. 4, pp. 392–397, Oct. 2005.

[8] L. Golestanirad, L. M. Angelone, M. I. Lacono, H. Katnani, L. L. Wald, and G. Bonmassar, "Local SAR near deep brain stimulation (DBS) electrodes at 64 and 127 MHz: A simulation study of the effect of extracranial loops," *Magn. Reson. Med.*, vol. 78, no. 4, pp. 1558–1565, Oct. 2017.

[9] J. Vu, B. Bhusal, J. M. Rosenow, J. Pilitsis, and L. Golestanirad, "Effect of surgical modification of deep brain stimulation lead trajectories on radiofrequency heating during MRI at 3T: From phantom experiments to clinical implementation," *J. Neurosurgery*, vol. 140, no. 5, pp. 1459–1470, May 2024.

[10] B. Bhusal et al., "Effect of device configuration and patient's body composition on the RF heating and nonsusceptibility artifact of deep brain stimulation implants during MRI at 1.5T and 3T," *J. Magn. Reson. Imag.*, vol. 53, no. 2, pp. 599–610, Feb. 2021.

[11] L. Golestanirad et al., "Construction and modeling of a reconfigurable MRI coil for lowering SAR in patients with deep brain stimulation implants," *NeuroImage*, vol. 147, pp. 577–588, Feb. 2017.

[12] B. Guerin et al., "Realistic modeling of deep brain stimulation implants for electromagnetic MRI safety studies," *Phys. Med. Biol.*, vol. 63, no. 9, May 2018, Art. no. 095015.

[13] L. Golestanirad et al., "RF-induced heating in tissue near bilateral DBS implants during MRI at 1.5 t and 3T: The role of surgical lead management," *NeuroImage*, vol. 184, pp. 566–576, Jan. 2019.

[14] L. Golestanirad et al., "Reconfigurable MRI coil technology can substantially reduce RF heating of deep brain stimulation implants: First in-vitro study of RF heating reduction in bilateral DBS leads at 1.5 T," *PLoS ONE*, vol. 14, no. 8, Aug. 2019, Art. no. e0220043.

[15] I. A. Elbakri and J. A. Fessler, "Statistical image reconstruction for polyenergetic X-ray computed tomography," *IEEE Trans. Med. Imag.*, vol. 21, no. 2, pp. 89–99, Feb. 2002.

[16] H. Yang et al., "Unsupervised MR-to-CT synthesis using structure-constrained CycleGAN," *IEEE Trans. Med. Imag.*, vol. 39, no. 12, pp. 4249–4261, Dec. 2020.

[17] K. B. Baker and M. D. Phillips, "Deep brain stimulation safety: MRI and other electromagnetic interactions," in *Deep Brain Stimulation Neurological Psychiatric Disorders*, D. Tarsy, J. L. Vitek, P. A. Starr, and M. S. Okun, Eds., Totowa, NJ, USA: Humana Press, 2008, pp. 453–472.

[18] H. Villarraga-Gómez, A. Amirkhanov, C. Heinzl, and S. T. Smith, "Assessing the effect of sample orientation on dimensional X-ray computed tomography through experimental and simulated data," *Measurement*, vol. 178, Jun. 2021, Art. no. 109343.

[19] P. J. Besl and R. C. Jain, "Invariant surface characteristics for 3D object recognition in range images," *Comput. Vis., Graph., Image Process.*, vol. 33, no. 1, pp. 33–80, Jan. 1986.

[20] G. Guennebaud and M. Gross, "Algebraic point set surfaces," *ACM Trans. Graph.*, vol. 26, no. 3, p. 23, Jul. 2007.

[21] A. O. Hebb and A. V. Poliakov, "Imaging of deep brain stimulation leads using extended Hounsfield unit CT," *Stereotactic Funct. Neurosurgery*, vol. 87, no. 3, pp. 155–160, 2009.

[22] P. Soille, *Morphological Image Analysis*. Berlin, Germany: Springer, 2004.

[23] R. C. Gonzalez, R. E. Woods, and S. L. Eddins, *Digital Image Processing Using MATLAB*, 3rd ed., Knoxville, TN, USA: Gatesmark Publishing, 2020.

[24] T. C. Lee, R. L. Kashyap, and C. N. Chu, "Building skeleton models via 3-D medial surface axis thinning algorithms," *CVGIP, Graph. Models Image Process.*, vol. 56, no. 6, pp. 462–478, Nov. 1994.

[25] M. Kerschnitzki et al., "Architecture of the osteocyte network correlates with bone material quality," *J. Bone Mineral Res.*, vol. 28, no. 8, pp. 1837–1845, Aug. 2013.

[26] D. Shepard, "A two-dimensional interpolation function for irregularly-spaced data," in *Proc. 23rd ACM Nat. Conf.*, 1968, pp. 517–524.